Article

Mixed-Valent Mn Supertetrahedra and Planar Discs as Enhanced Magnetic Coolers

Maria Manoli, Anna Collins, Simon Parsons, Andrea Candini, Marco Evangelisti, and Euan K. Brechin

J. Am. Chem. Soc., **2008**, 130 (33), 11129-11139 • DOI: 10.1021/ja802829d • Publication Date (Web): 25 July 2008

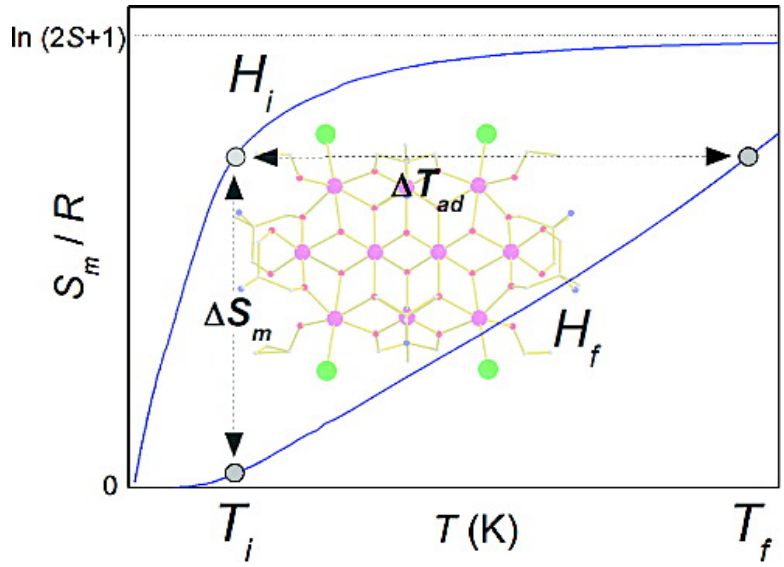

More About This Article

Additional resources and features associated with this article are available within the HTML version:

- Supporting Information
- Links to the 1 articles that cite this article, as of the time of this article download
- Access to high resolution figures
- Links to articles and content related to this article
- Copyright permission to reproduce figures and/or text from this article

View the Full Text HTML

J|A|C|S
ARTICLES

Published on Web 07/25/2008

Mixed-Valent Mn Supertetrahedra and Planar Discs as Enhanced Magnetic Coolers

Maria Manoli,[†] Anna Collins,[†] Simon Parsons,[†] Andrea Candini,[‡] Marco Evangelisti,*[,‡] and Euan K. Brechin*[,†]

School of Chemistry, The University of Edinburgh, West Mains Road, Edinburgh, EH9 3JJ U.K., and CNR-INFM National Research Center on "nanoStructures and bioSystems at Surfaces" (S³), Via G. Campi 213/A, 41100 Modena, Italy

Received April 17, 2008; E-mail: ebrechin@staffmail.ed.ac.uk; evange@unimore.it

Abstract: The syntheses and structures of two decametallic mixed-valent Mn supertetrahedra using 2-amino-2-methyl-1,3-propanediol ($ampH_2$), two decametallic mixed-valent Mn planar discs using 2-amino-2-methyl-1,3-propanediol ($ampH_2$) and 2-amino-2-ethyl-1,3-propanediol ($aepH_2$), and a tetradecametallic mixed-valent Mn planar disc using pentaerythritol (H_4peol) are reported. The decametallic complexes display dominant ferromagnetic exchange and spin ground states of $S = 22$, and the tetradecametallic complex displays dominant antiferromagnetic exchange and a spin ground state of $S = 7 \pm 1$. All display large (the former) and enormous (the latter) magnetocaloric effect—the former as a result of negligible zero-field splitting of the ground state, and the latter as a result of possessing a high spin-degeneracy at finite low temperatures—making them the very best cooling refrigerants for low-temperature applications.

Introduction

Polymetallic complexes of paramagnetic transition metals possessing large spin ground states are of interest since they can display either single-molecule magnetism behavior[1] or an enhanced magnetocaloric effect (MCE).[2] The latter describes the change of magnetic entropy (ΔS_m) following a change of the applied magnetic field (ΔH) and has potential technological use in cooling applications.[3] Although the MCE is intrinsic to any magnetic material, in only a few cases is the ΔS_m sufficiently large to make the materials suitable for applications. The key is to find the best performing refrigerant.

The magnetocaloric effect and the related principle of magnetic refrigeration are summarized in Figure 1. A spin S has a $2S + 1$ degeneracy in zero-field; hence, the full amount of the magnetic entropy S_m is $R \ln(2S + 1)$, where R is the gas constant. On application of a magnetic field H, this degeneracy is lifted, the spin system orders, and $S_m(T,H)$ decreases (S_m is nil on saturation of the magnetization). Therefore, if a magnetic field H_f is applied to the sample, in thermal equilibrium with a heat bath and at initial temperature T_i and field H_i (say, $H_i = 0$), we isothermally decrease the magnetic entropy ΔS_m (vertical arrow in Figure 1). If alternatively the sample is thermally isolated and the field changed to H_f in a reversible process, we perform an adiabatic magnetization. When the total entropy of the system remains constant during the magnetic field change ΔH, the magnetic entropy change must be compensated for by

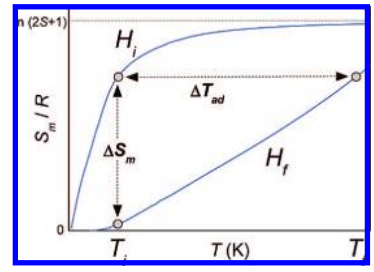

Figure 1. Magnetic entropy (S_m) as a function of temperature (T) for two different applied magnetic fields H_i and H_f, where $H_i < H_f$. Indicated are the magnetic entropy change ΔS_m following an isothermal $\Delta H = H_f - H_i$ (vertical arrow), and the temperature change $\Delta T_{ad} = T_f - T_i$ for ΔH under adiabatic conditions (horizontal arrow).

an equal but opposite change of the entropy associated with the lattice, resulting in a change in temperature ΔT_{ad} of the material (horizontal arrow in Figure 1). It is easy to see that if ΔH reduces the entropy ($\Delta S_m < 0$), then ΔT_{ad} is positive, whereas if ΔH is such that $\Delta S_m > 0$, then $\Delta T_{ad} < 0$.

High-spin molecules are thus good candidates for magnetic refrigeration, since high values of the spin are needed to achieve respectively large magnetic entropies, which may lead to large magnetocaloric effects.[4] In addition, a large MCE is also obtained whenever relatively small ΔH values are sufficient to fully change the polarization of the magnetic molecules, and this requires the anisotropy of the molecules to be negligible.[2] The search for high-spin isotropic molecules led us to the $[Fe_{14}]$, $[Fe_{17}]$, and $[Mn_{10}]$ molecules that have shown much promise in this regard.[5] Notably, we observed MCEs that are comparable and *even larger* than those reported for the best intermetallic

[†] The University of Edinburgh.
[‡] CNR-INFM National Research Center, S³.

(1) Gatteschi, D.; Sessoli, R.; Villain, J. *Molecular Nanomagnets*; Oxford University Press: Oxford, UK, 2006.
(2) Evangelisti, M.; Luis, F.; de Jongh, L. J.; Affronte, M. *J. Mater. Chem.* **2006**, *16*, 2534–2549.
(3) Pecharsky, V. K.; Gschneidner, K. A., Jr. *J. Magn. Magn. Mater.* **1999**, *200*, 44–56.
(4) Spichkin, Yu, I.; Zvezdin, A. K.; Gubin, S. P.; Mischenko, A. S.; Tishin, A. M. *J. Phys. D: Appl. Phys.* **2001**, *34*, 1162–1166.

and lanthanide alloys conventionally studied and employed for low-temperature cooling applications. The challenge is to find ways of enhancing the MCE even further. Adding low-lying (hence accessible) spin states other than the ground state is, for instance, an efficient method for increasing the degrees of freedom of the system, leading to an excess of magnetic entropy. In terms of MCE, the efficiency of a magnetic system with degenerate spin states can theoretically exceed that of an equivalent (super)paramagnet by more than an order of magnitude.[6] The molecular energy scheme, in particular the presence of low-lying excited spin states, is determined by the nature of the intramolecular magnetic interactions and can be induced by either promoting frustration or (more simply) generating relatively weak exchange interactions. In what follows, we report the very large MCE of an isotropic, ferromagnetic, manganese-based molecule with a well-defined spin ground state. We then make a similar molecule in which the bridging oxides holding the metallic core together have been replaced with bridging hydroxides, promoting weaker pairwise exchange—this leads to an enhanced MCE. We then make a third molecule that contains a higher ratio of Mn^{2+} ions, creating new, weak, and antiferromagnetic $Mn^{2+}-Mn^{2+}$ interactions. This results in a truly *enormous* enhancement of the MCE, making these molecules the very best refrigerants for low-temperature (below ~10 K) applications ever reported.

Recent years have witnessed great research activity in the chemistry of polymetallic manganese complexes, partly because of their relevance to the Mn_4 cluster at the water oxidation center of photosystem II,[7] and partly because some of them behave as nanoscale magnets (single-molecule magnets, SMMs), the latter having potential uses in information storage and quantum computation.[8] Mn is particularly useful for obtaining molecules with large S values—its ability to exist in numerous oxidation states means even antiferromagnetic exchange will often lead to complexes possessing nonzero spin ground states. Indeed, the vast majority of published SMMs are mixed-valent Mn complexes.[9] Such species come in a bewildering variety of shapes and sizes, from simple triangles, cubes, and butterflies to wheels, discs, rods, truncated cubes, supercubanes, and supertetrahedra to the beautifully unusual and irregular.[10] Most are made through self-assembly via the simple combination of Mn^{2+} salts or $[Mn_3O(O_2CR)_6L_3]^{n+}$ triangles with flexible bridging/chelating ligands. In recent years, we have been investigating the coordination chemistry of the tripodal alcohols H_3thme, H_3tmp, H_4peol, and their analogues (Scheme 1) with transition metal ions, with a particular focus on Mn.[11] When fully deprotonated, these ligands direct the formation of triangular Mn_3 units, where each oxygen atom bridges one edge of the triangle. In the presence of other bridging/chelating ligands, such as carboxylates or β-diketonates, these triangles

Scheme 1. Structures of 1,1,1-Tris(hydroxymethyl)ethane (H_3thme), 1,1,1-Tris(hydroxymethyl)propane (H_3tmp), Pentaerythritol (H_4peol), 2-Amino-2-methyl-1,3-propanediol ($ampH_2$), and 2-Amino-2-ethyl-1,3-propanediol ($aepH_2$)

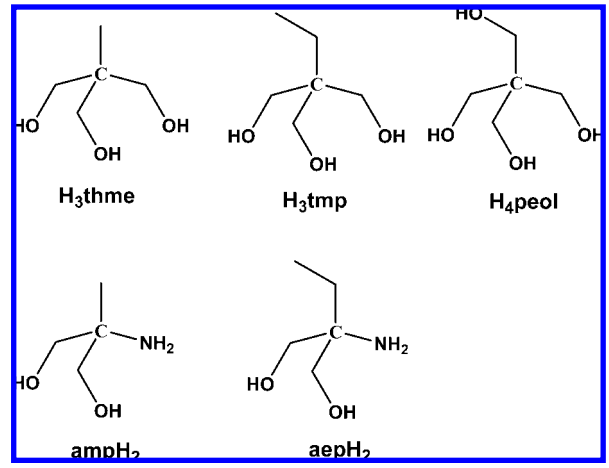

self-assemble to give a plethora of polymetallic clusters commonly based on rods, discs, tetrahedra, octahedra, and icosahedra.[11] A natural extension to these studies is the investigation of the coordination chemistry of analogous organic molecules in which one (or more) of the alcohol "arms" is replaced by an alternative functional group(s), for example, an amine group.[12] While each alkoxide arm has the potential to bridge up to three metals (and thus a maximum of seven metals per tripodal ligand), the $-NH_2$ "arm" is likely, if bonded, to act solely as a monodentate/terminal capping unit and should give rise to a number of related, yet different, structural topologies.

(5) (a) Evangelisti, M.; Candini, A.; Ghirri, A.; Affronte, M.; Brechin, E. K.; McInnes, E. J. L. *Appl. Phys. Lett.* **2005**, *87*, 072504. (b) Evangelisti, M.; Candini, A.; Ghirri, A.; Affronte, M.; Piligkos, S.; Brechin, E. K.; McInnes, E. J. L. *Polyhedron* **2005**, *24*, 2573–2578. (c) Manoli, M.; Johnstone, R. D. L.; Parsons, S.; Murrie, M.; Affronte, M.; Evangelisti, M.; Brechin, E. K. *Angew. Chem., Int. Ed.* **2007**, *46*, 4456–4460. (d) Shaw, R. S.; Laye, R. H.; Jones, L. F.; Low, D. M.; Talbot-Eeckelaers, C.; Wei, Q.; Milios, C. J.; Teat, S.; Helliwell, M.; Raftery, J.; Evangelisti, M.; Affronte, M.; Collison, D.; Brechin, E. K.; McInnes, E. J. L. *Inorg. Chem.* **2007**, *46*, 4968–4978.
(6) Zhitomirsky, M. E. *Phys. Rev. B* **2003**, *67*, 104421.
(7) (a) *Manganese Redox Enzymes*; Pecoraro, V. L.; Ed.; VCH Publishers: New York, 1992. (b) Christou, G. *Acc. Chem. Res.* **1989**, *22*, 328–335.
(8) Gatteschi, D.; Sessoli, R. *Angew. Chem., Int. Ed.* **2003**, *42*, 268–297.
(9) Aromí, G.; Brechin, E. K. *Struct. Bonding (Berlin)* **2006**, *122*, 1–68.
(10) See for example: (a) Cannon, R. D.; White, R. P. *Prog. Inorg. Chem.* **1988**, *36*, 195–297. (b) Aubin, S. M. J.; Dilley, N. R.; Wemple, M. W.; Maple, M. B.; Christou, G.; Hendrickson, D. N. *J. Am. Chem. Soc.* **1998**, *120*, 839–840. (c) Yoo, J.; Brechin, E. K.; Yamaguchi, A.; Nakano, M.; Huffman, J. C.; Maniero, A. L.; Brunel, L. C.; Awaga, K.; Ishimoto, H.; Christou, G.; Hendrickson, D. N. *Inorg. Chem.* **2000**, *39*, 3615–3623. (d) Tasiopoulos, A. T.; Vinslava, A.; Wernsdorfer, W.; Abboud, K. A.; Christou, G. *Angew. Chem., Int. Ed.* **2004**, *43*, 2117–2121. (e) Koizumi, S.; Nihei, M.; Nakano, M.; Oshio, H. *Inorg. Chem.* **2005**, *44*, 1208–1210. (f) Rajaraman, G.; Murugesu, M.; Sanudo, E. C.; Soler, M.; Wernsdorfer, W.; Helliwell, M.; Muryn, C.; Raftery, J.; Teat, S. J.; Christou, G.; Brechin, E. K. *J. Am. Chem. Soc.* **2004**, *126*, 15445–15457. (g) Scott, R. T. W.; Parsons, S.; Murugesu, M.; Wernsdorfer, W.; Christou, G.; Brechin, E. K. *Angew. Chem., Int. Ed.* **2005**, *44*, 6540–6543. (h) Sun, Z.; Gantzel, P. K.; Hendrickson, D. N. *Inorg. Chem.* **1996**, *35*, 6640–6641. (i) Ferguson, A.; Thomson, K.; Parkin, A.; Cooper, P.; Milios, C. J.; Brechin, E. K.; Murrie, M. *Dalton Trans.* **2007**, 728–729. (j) Murugesu, M.; Habrych, M.; Wernsdorfer, W.; Abboud, K. A.; Christou, G. *J. Am. Chem. Soc.* **2004**, *126*, 4766–4767. (k) Soler, M.; Wernsdorfer, W.; Folting, K.; Pink, M.; Christou, G. *J. Am. Chem. Soc.* **2004**, *126*, 2156–2165. (l) Jones, L. F.; Rajaraman, G.; Brockman, J.; Murugesu, M.; Sanudo, E. C.; Raftery, J.; Teat, S. J.; Wernsdorfer, W.; Christou, G.; Brechin, E. K.; Collison, D. *Chem. Eur. J.* **2004**, *10*, 5180–5194. (m) Stamatatos, T. C.; Abboud, K. A.; Wernsdorfer, W.; Christou, G. *Angew. Chem., Int. Ed.* **2006**, *45*, 4134–4137, and references therein. (n) Rumberger, E. M.; Zakharov, L. N.; Rheingold, A. L.; Hendrickson, D. N. *Inorg. Chem.* **2004**, *43*, 6531–6533. (o) Zhou, A.-J.; Qin, L.-J.; Beedle, C. C.; Ding, S.; Nakano, M.; Leng, J.-D.; Tong, M.-L.; Hendrickson, D. J. *Inorg. Chem.* **2007**, *46*, 8111–8113. (p) Bagai, R.; Abboud, K. A.; Christou, G. *Inorg. Chem.* **2008**, *47*, 621–631.
(11) Brechin, E. K. *Chem. Commun.* **2005**, 5141–5153.
(12) The coordination chemistry of $aepH_2$ and $ampH_2$ is largely unexplored. For other polymetallic complexes based on these ligands, see: (a) Milios, C. J.; Manoli, M.; Mishra, A.; Budd, L. E.; White, F.; Parsons, S.; Christou, G.; Wernsdorfer, W.; Brechin, E. K. *Inorg. Chem.* **2006**, *45*, 6782–6793. (b) Alley, K. G.; Bircher, R.; Waldmann, O.; Ochsenbein, S. T.; Güdel, H. U.; Moubaraki, B.; Murray, K. S.; Fernandez-Alonso, F.; Abrahams, B. F.; Boskovic, C. *Inorg. Chem.* **2006**, *45*, 8950–8957.

Table 1. X-ray Crystallographic Data and Refinement Parameters for **1**−**5**

	1·8hex	**2**·5hex	**3**·12EtOH	**4**·6EtOH	**5**
formula	$C_{88}H_{212}Mn_{10}Br_7N_{10}O_{24}$	$C_{70}H_{169.8}Mn_{10}I_{7.2}N_{10}O_{25.8}$	$C_{64}H_{162}Mn_{10}I_8N_8O_{38}$	$C_{56}H_{148}Mn_{10}I_8N_8O_{32}$	$C_{58}I_8Mn_{14}O_{48}$
M_w	2903.41	3027.75	3216.64	3010.34	2663.71
crystal system	rhombohedral	trigonal	monoclinic	rhombohedral	monoclinic
space group	$R\bar{3}$	$R\bar{3}$	$P\bar{1}21/n1$	$Pbcn$	$P\bar{1}21/n1$
a/Å	15.6083(4)	15.8200(3)	25.6712(10)	25.5208(6)	13.1676(4)
b/Å	15.6083(4)	15.8200(3)	17.0984(7)	16.2775(4)	22.4000(6)
c/Å	76.462(5)	77.614(3)	26.2611(11)	26.0702(6)	21.4912(6)
α/°	90	90	90	90	90
β/°	90	90	96.036(2)	90	91.920(2)
γ/°	120	120	90	90	90
V/Å^3	16132.0(1)	16822.2(8)	11463.0(8)	10829.9(4)	6335.4(3)
Z	6	6	4	4	4
T/K	150(2)	150(2)	150(2)	150(2)	150(2)
λ/Å	0.71073	0.71073	0.71073	0.71073	0.71073
D_c/g cm^{-3}	1.606	1.79	1.543	1.85	1.70
μ(Mo Kα)/mm^{-1}	2.319	3.132	3.265	3.471	3.357
meas/indep(R_{int}) reflns	58941/7364(0.066)	11323/11323(0.047)	35196/35196 (0.068)	16047/16047(0.062)	16848/16848(0.079)
wR2	0.1305	0.0812	0.1610	0.1531	0.3949
R1	0.0464	0.0779	0.0580	0.0629	0.2025
goodness of fit on F^2	1.051	1.0139	0.8972	0.8833	1.0398

Here we report the syntheses and structures of two decametallic mixed-valent Mn supertetrahedra using 2-amino-2-methyl-1,3-propanediol ($ampH_2$),[5c] two decametallic mixed-valent Mn planar discs using 2-amino-2-methyl-1,3-propanediol ($ampH_2$) and 2-amino-2-ethyl-1,3-propanediol ($aepH_2$), and a tetradecametallic mixed-valent Mn planar disc using pentaerythritol (H_4peol). The decametallic complexes display dominant ferromagnetic exchange and spin ground states of $S = 22$, and the tetradecametallic complex displays dominant antiferromagnetic exchange and a spin ground state of $S = 7 \pm 1$. All display large (the former) and enormous (the latter) MCE, the former as a result of negligible zero-field splitting of the ground state, and the latter as a result of possessing a high spin-degeneracy at finite low temperatures.

Materials and Physical Measurements

All manipulations were performed under aerobic conditions using materials as received (reagent grade). Variable-temperature, solid-state direct current (dc) and alternating current (ac) magnetic susceptibility data down to 1.8 K were collected on Quantum Design MPMS-XL SQUID and PPMS magnetometers, each equipped with a 7 T dc magnet. Diamagnetic corrections were applied to the observed paramagnetic susceptibilities using Pascal's constants. Specific heat experiments down to 0.3 K and up to 7 T were carried out with the PPMS. Magnetization and susceptibility measurements below 2 K were performed using homemade Hall microprobes. In this case, the grain-like samples consisted of collections of small crystallites of ca. 10^{-3} mm^3. For measurements performed on powder samples, the calculated fits were obtained taking into account random spin orientations.

X-ray Crystallography and Structure Solution. Diffraction data were collected at 150 K on a Bruker Smart Apex CCDC diffractometer, equipped with an Oxford Cryosystems LT device, using Mo radiation. See Table 1 and CIF files (CCDC 639301, 671791−671793) for full details. Data for **5** were of insufficient quality to allow full structure analysis but were suitable for the structure, connectivity, and formula to be confirmed. Unit cell details are given in Table 1 for completeness. All CIF files are included in the Supporting Information.

Synthetic Procedures. $[Mn^{III}_6Mn^{II}_4O_4Br_4(amp)_6(ampH_2)_3(HampH_2)]Br_3$·8hex (1·8hex). $MnBr_2$·$4H_2O$ (500 mg, 1.74 mmol) and $ampH_2$ (184 mg, 1.74 mmol) were stirred in MeOH for 1 h. The solution was then filtered and layered with hexanes. Crystals of **1**·8hex formed in 3 days in a yield of approximately 20%. Anal. Calcd (found) for **1**·2.5hex, $C_{55}H_{135}Mn_{10}N_{10}Br_7O_{24}$: C 26.84 (26.98), H 5.53 (5.49), N 5.69 (5.49).

$[Mn^{III}_6Mn^{II}_4O_4(OH)_{1.8}I_{2.2}(amp)_6(ampH_2)_1(HampH_2)_3]I_5$·5hex (2·5hex). To a stirred MeOH solution of MnI_2 (500 mg, 1.62 mmol) and tertabutylammonium iodide (TBAI: 598 mg, 1.62 mmol) was added $ampdH_2$ (170 mg, 1.62 mmol). After 3 h the solution was filtered and layered with hexanes. Crystals of **2**·5hex formed in 10 days in a yield of approximately 25%. Anal. Calcd (found) for **2**·4hex, $C_{64}H_{155.8}Mn_{10}I_{7.2}N_{10}O_{25.8}$: C 27.19 (27.08), H 5.60 (5.54), N 5.77 (5.71).

$[Mn^{III}_6Mn^{II}_4(OH)_6(amp)_4(ampH)_4I_4(EtOH)_4]I_4$·12EtOH (3·12EtOH). MnI_2 (500 mg, 1.62 mmol) and $ampH_2$ (170 mg, 1.62 mmol) were stirred in EtOH for 5 h. The solution was then filtered and layered with hexane, producing crystals of **3** during 5 days in a yield of approximately 30%. Anal. Calcd (found) for **3**, $C_{40}H_{90}Mn_{10}N_8I_8O_{26}$: C 18.04 (17.99), H 3.41 (3.90), N 4.21 (3.93).

$[Mn^{III}_6Mn^{II}_4(OH)_6(aep)_4(aepH)_4I_4(EtOH)_4]I_4$·6EtOH (4·6EtOH). MnI_2 (500 mg, 1.62 mmol) and $aepH_2$ (193 mg, 1.62 mmol) were stirred in EtOH for 5 h. The solution was then filtered and layered with hexane, producing crystals of **4** during 10 days in a yield of approximately 30% yield. Anal. Calcd (found) for **4**,$C_{44}H_{98}Mn_{10}N_8I_8O_{26}$: C 19.43 (19.52), H 3.63 (4.07), N 4.12 (3.94).

$[Mn^{III}_6Mn^{II}_8(OH)_2(Hpeol)_4(H_2peol)_6I_4(EtOH)_6]I_4$ (5). MnI_2 (500 mg, 1.62 mmol) and H_4peol (220 mg, 1.62 mmol) were stirred in EtOH for 5 h. The solution was then filtered and layered with hexane. Crystals of **5** formed in 8 days in a yield of approximately 15%. Anal. Calcd (found) for **5**, $C_{58}H_{126}Mn_{14}I_8O_{48}$: C 20.64 (20.73), H 3.76 (3.71).

Results and Discussion

Synthesis. Reaction of $MnBr_2$·$4H_2O$ with 1 equiv of 2-amino-2-methyl-1,3-propanediol ($ampH_2$) affords the mixed-valent supertetrahedron $[Mn_{10}O_4Br_4(amp)_6(ampH_2)_3(HampH_2)]Br_3$ (**1**). When the reaction is repeated replacing $MnBr_2$·$4H_2O$ with MnI_2 in the presence of TBAI, the analogous complex $[Mn_{10}O_4(OH)_{1.8}I_{2.2}(amp)_6(ampH_2)_1(HampH_2)_3]I_5$ (**2**) forms. If the latter reaction is repeated in EtOH instead of MeOH, the planar complex $[Mn_{10}(OH)_6(amp)_4(ampH)_4I_4(EtOH)_4]I_4$ (**3**) forms. If

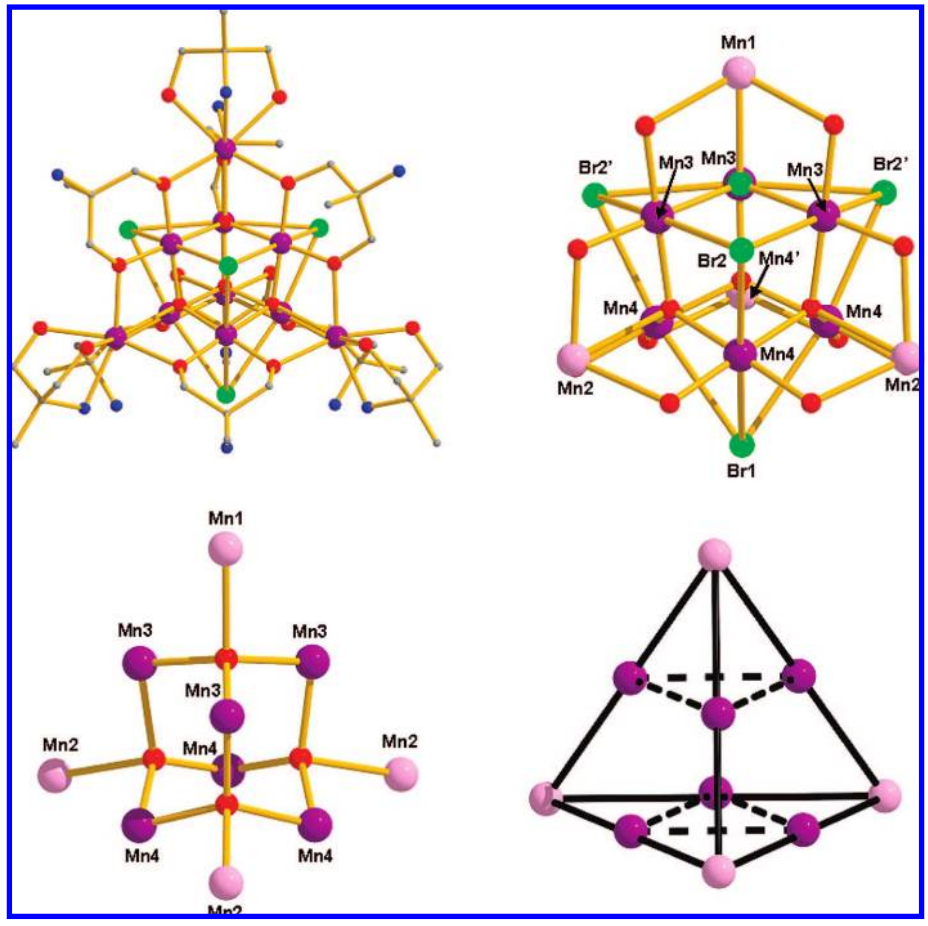

Figure 2. Molecular structure of **1** (top) and its supertetrahedral core and metallic skeleton (bottom). Color code: Mn, purple; O, red; N, blue; Br, green; C, gray. In the bottom pictures, the Mn^{3+} ions are purple and the Mn^{2+} ions pink.

Table 2. Selected Interatomic Distances (Å) and Angles (°) for **1**−**5**

complex	Mn^{3+}−O^{2-}	Mn^{2+}−O^{2-}	Mn^{3+}−OH^{-}	Mn^{2+}−OH^{-}	Mn^{3+}−halide^{-}	Mn^{2+}−halide
1	1.896−1.933	2.225−2.304			2.771−2.963	
2	1.901−1.922	2.260−2.277			2.962−3.228	
3			1.870−2.293	2.284−2.293		2.804−2.821
4			1.862−2.325	2.280−2.290		2.775−2.832
5				2.118−2.180		2.815−2.858

complex	Mn^{3+}−O^{2-}−Mn^{3+}	Mn^{3+}−O^{2-}−Mn^{2+}	Mn^{3+}−OH−Mn^{3+}	Mn^{3+}−OH−Mn^{2+}	Mn^{2+}−OH−Mn^{2+}	Mn^{3+}−halide−Mn^{3+}
1	112.86−121.78	100.54−103.07				68.26−69.44
2	111.13−123.33	101.21−103.04				62.93−64.17
3			95.75−102.51	93.34−105.72		
4			95.76−102.31	92.36−105.59		
5					98.66−100.65	

$ampH_2$ is replaced with 2-amino-2-ethyl-1,3-propanediol ($aepH_2$) in the equivalent reaction, the analogous complex $[Mn_{10}(OH)_6(aep)_4(aepH)_4I_4(EtOH)_4]I_4$ (**4**) results, but when replaced with pentaerythritol (H_4peol), the tetradecametallic $[Mn_{14}(OH)_2(Hpeol)_4(H_2peol)_6I_4(EtOH)_6]I_4$ (**5**) forms.

It is difficult to speculate on the reaction pathways that lead to the formation of the five complexes, but an examination of their structures shows that they are clearly all related. In particular, the differences between the decametallic supertetrahedra and the decametallic discs are minimal—both contain $[Mn^{III}_6Mn^{II}_4]$ cores in which each metal ion has a nearest neighbor of different oxidation state, surrounded by 8−10 ligands bridging in a similar fashion. The major change appears to be the presence of oxides in the central cores of the supertetrahedra and hydroxides in the planar discs. The former are tetrahedral and form four bonds, whereas the latter are pyramidal/pseudoplanar and form three bonds; i.e., the oxides template the formation of "3D" tetrahedra and the hydroxides template the formation of "2D" planar discs. The formation of the larger tetradecametallic disc **5** in comparison to the decametallic discs can be attributed to the change in bridging ligand. While the anions of $ampH_2$ and $aepH_2$ tend to bridge around the periphery of the clusters, the anions of tripodal alcohols such as H_4peol tend to sit directly above and below the centers of planar cores.[11] The presence of three alkoxide arms allows for greater coordination than two alkoxides and one amine. For example, the tetradecametallic complex **5** contains four centrally located $Hpeol^{3-}$ anions, each bridging in a μ_6-fashion encom-

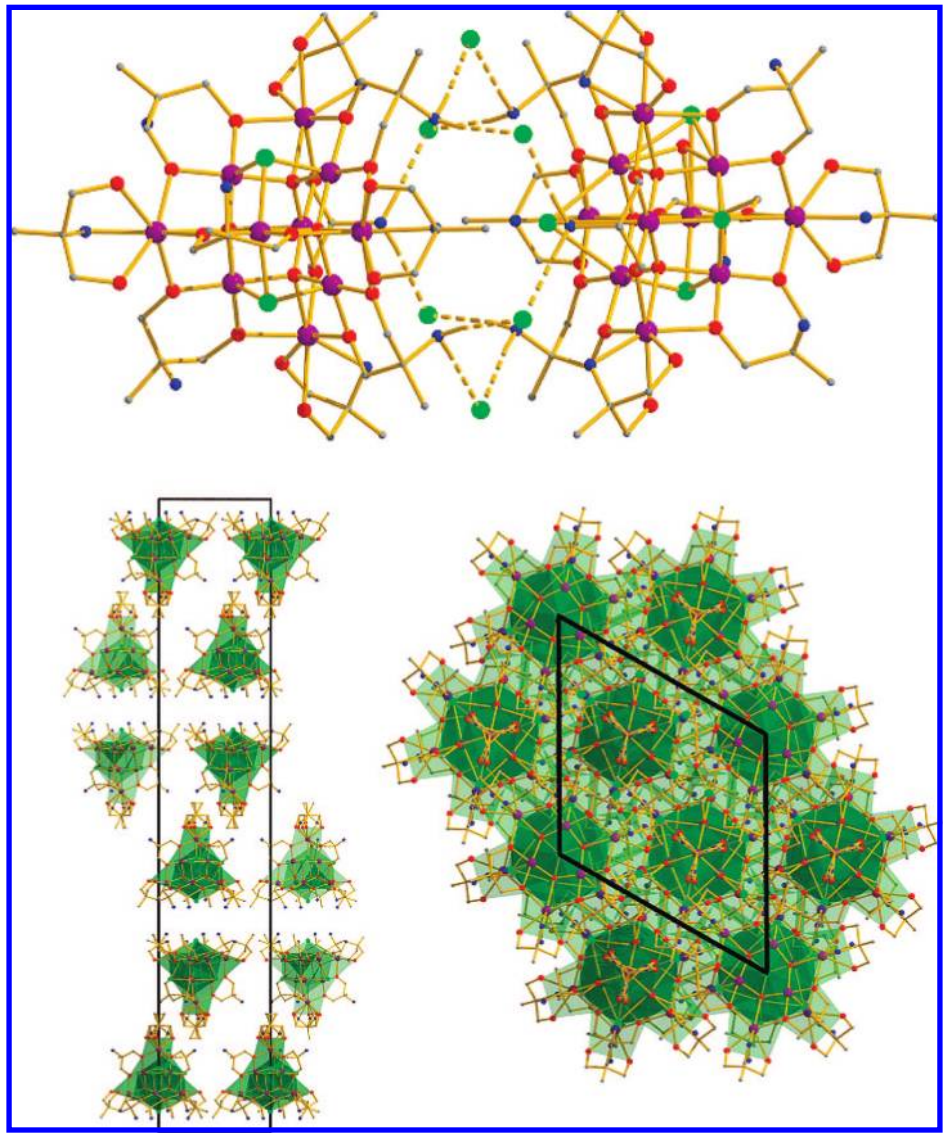

Figure 3. (Top) Head-to-head $[Mn_{10}]_2$ dimers found in the crystal of **1** and **2**, and (bottom) the packing of the molecules in the crystal viewed down the *b* (left) and *c* (right) axes.

passing a total of 10 central metal ions, while the largest coordination mode seen for the anions of $ampH_2$ and $aepH_2$ is μ_5, occurring only twice in **3** and **4** and encompassing a total of eight metal ions.

Description of Structures. Since complexes **1**-**2** and **3**-**4** have analogous structures, and for the sake of brevity, we will limit our discussion to **1**, **3**, and **5**. $[Mn_{10}O_4Br_4(amp)_6(ampH_2)_3(HampH_2)]Br_3$ (**1**) crystallizes in the rhombohedral space group $R\bar{3}$ (Figure 2; selected bond lengths and angles are given in Table 2). The $[Mn_{10}]^{3+}$ cation contains a metallic skeleton that describes a mixed-valent $[Mn^{III}_6Mn^{II}_4]$ supertetrahedron (Mn1, Mn2 = 2+; Mn3, Mn4 = 3+) in which each nearest neighbor is of a different oxidation state (Figure 2). The Mn^{2+} ions define the four apexes of the tetrahedron, with the Mn^{3+} ions lying along each edge. The Mn^{3+} ions themselves, therefore, describe a trigonal antiprism. The metal ions are connected by four central tetrahedral oxide ions to give a $[Mn^{III}_6Mn^{II}_4O_4]^{18+}$ core such that the supertetrahedron can be thought of as being built from four vertex-sharing $[Mn^{III}_3Mn^{II}O]^{9+}$ tetrahedra. The four bromide ions each cap one face of the tetrahedron. The tripodal ligands are of two types: six are doubly deprotonated (amp^{2-}), bridging in an $\eta^2{:}\eta^2{:}\mu_3$-fashion along each edge of the tetrahedron, and four remain fully protonated ($ampH_2$), chelating each Mn^{2+} vertex ion.

The pendant $-NH_2$ "arms" of the amp^{2-} ligands at the triangular "base" of the cluster are H-bonded to Br^- counterions that lie between neighboring $[Mn_{10}]$ molecules. Each N-atom is H-bonded to two Br^- ions at distances of approximately 3.2 Å, forming head-to-head $[Mn_{10}]_2$ dimers throughout the crystal (Figure 3). The Jahn−Teller axes of the octahedral Mn^{3+} ions are directed by the presence of the long Mn−Br bonds; thus, for Mn4 their direction is defined by Br1 and Br2, and for Mn3 their direction is defined by Br2 and symmetry equivalent. All the Mn^{2+} ions are seven-coordinate, bound to a $\{O_6N\}$ set of atoms. Triply bridging Br^- (halide) ions have been seen before in Mn chemistry, in the complexes: $[Mn_4O_3X(O_2CR)_3(dbm)_3]$ (X = halide, Hdbm = dibenzoylmethane), in which the halide sits in the corner of a distorted cubane; $[Mn_6O_4Br_4(R_2dbm)_6]$, in which the halide caps the face of an octahedron; and $[NMe_4]_4[Mn_{10}O_4(biphen)_4Br_{12}]$ (biphen = 2,2′-biphenoxide), in

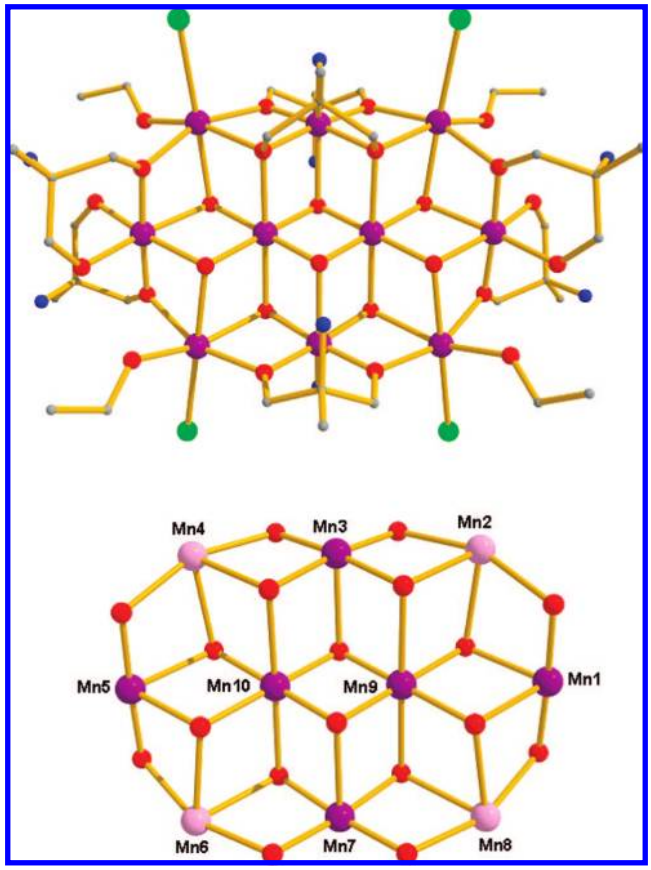

Figure 4. Molecular structure of **3** (top) and its metal−oxygen core (bottom). Color code as in Figure 2.

which the μ_3-halides form an $\{Mn_4Br_6\}$ adamantane-like core.[13] In each of these complexes, the μ_3-Br^- ions sit on an axially elongated site with average Mn^{3+}−Br distances in the range ∼2.79−2.84 Å, consistent with the values seen here (Mn−Br(av) = 2.82 Å). The charge balance of the complex is completed by the presence of the Br^- counterions and an additional proton. Significant disorder within the $[Mn_{10}]$ unit and in the interstitial solvent molecules (see CIF files in the Supporting Information for full details) makes knowing its exact location difficult, though we have assumed it is disordered over the (basal) $-NH_2$ moieties. Complex **2** has an analogous structure, but the capping halides are disordered with hydroxide ions in a 2.2:1.8 ratio. The presence of a fifth halide counterion leads to an overall formulation of $[Mn_{10}O_4(OH)_{1.8}I_{2.2}(amp)_6(ampH_2)_1(ampH_2)_3]I_5$. Again, the halide counterions lie between neighboring clusters in the crystal, H-bonding to the $-NH_2$ moieties and creating $[Mn_{10}]_2$ dimers. When viewed down the *c*-axis, these dimers form aesthetically pleasing "hexagonal" columns (Figure 3). The closest intermolecular Mn···Mn distances are ∼9.4 and ∼9.8 Å for **1** and **2**, respectively.

$[Mn_{10}(OH)_6(amp)_4(ampH)_4I_4(EtOH)_4]I_4$ (**3**) crystallizes in the monoclinic space group *P*21/*n* (Figure 4; selected bond lengths and angles are given in Table 2). The Mn−O core of **3** describes a planar disc of 10 Mn ions linked by six central μ_3-OH^- ions,

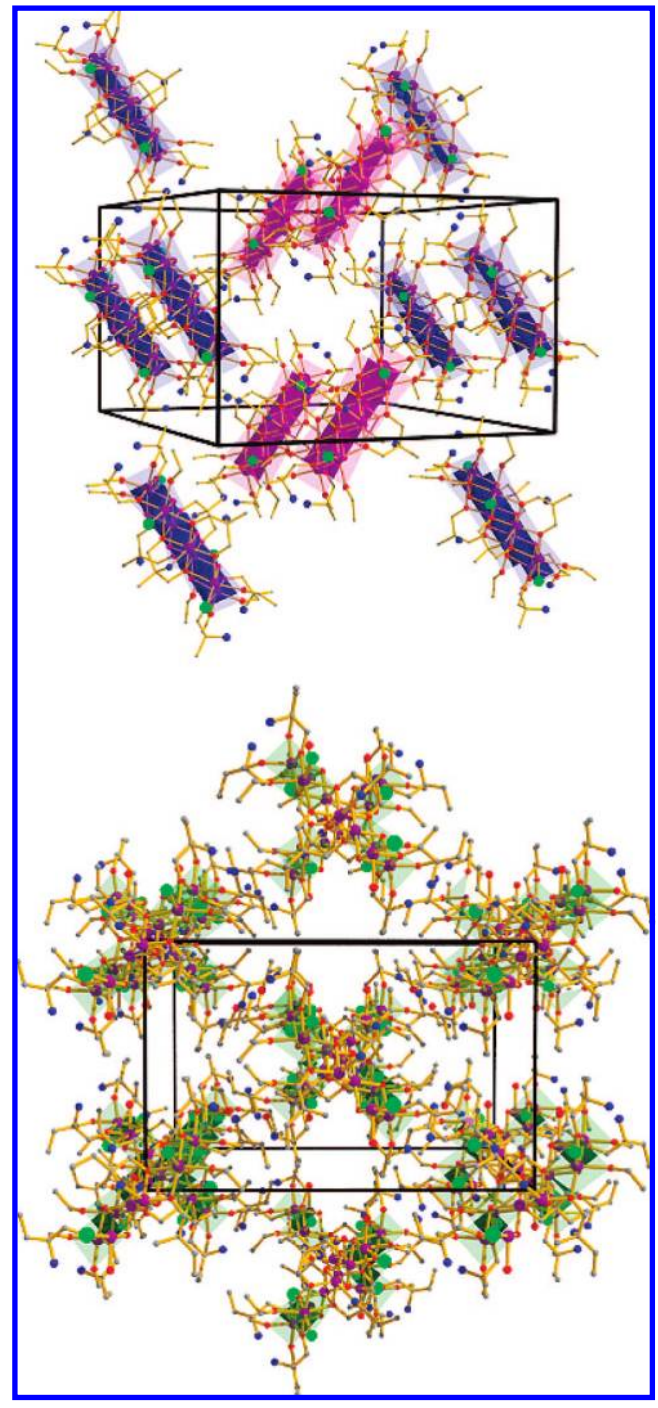

Figure 5. Packing of **3** (top) and **4** (bottom) in the crystal.

forming a central $[Mn^{III}_6Mn_4^{II}(OH)_6]^{20+}$ core (Figure 4). The metallic skeleton thus comprises 10 edge-sharing triangles which form a "2D planar disc". The tripodal ligands bridge in three distinct ways. The four central ligands are doubly deprotonated (amp^{2-}) and bridge in two ways: two in an η^3:η^3:η^1:μ_5-fashion, and two in an η^2:η^2:μ_3-fashion. The four peripheral ligands are singly deprotonated ($ampH^-$), each bridging in an η^2:η^1:μ-fashion. Four terminally bound I^- ions and four EtOH molecules fill the vacant coordination sites on the Mn^{2+} ions. The Mn^{3+} ions are six-coordinate and in distorted octahedral geometries but, unusually, show two distinct geometries: Mn3, Mn7, Mn9, and Mn10 display the usual axial elongation, but Mn1 and Mn5 are axially compressed. There are a significant number of intra-

(13) (a) Wang, S.; Tsai, H.-L.; Libby, E.; Folting, K.; Streib, W. E.; Hendrickson, D. N.; Christou, G. *Inorg. Chem.* **1996**, *35*, 7578–7589. (b) Aromí, G.; Knapp, M. J.; Claude, J.-P.; Huffman, J. C.; Hendrickson, D. N.; Christou, G. *J. Am. Chem. Soc.* **1999**, *121*, 5489–5499. (c) Goldberg, D. P.; Caneschi, A.; Delfs, C. D.; Sessoli, R.; Lippard, S. J. *J. Am. Chem. Soc.* **1995**, *117*, 5789–5800.

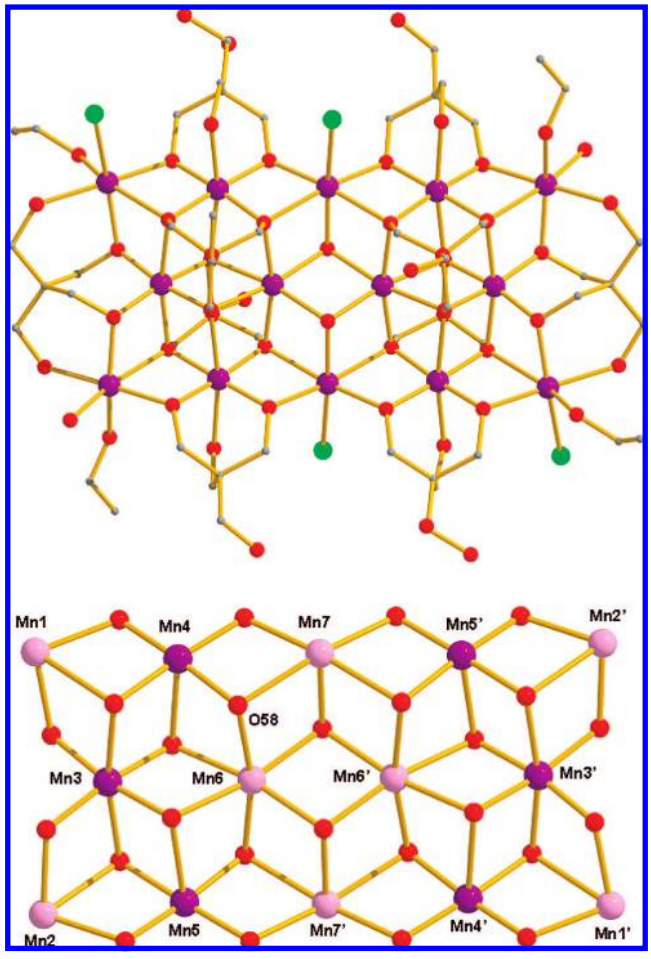

Figure 6. Molecular structure of **5** (top) and its metal−oxygen core (bottom). Color code as Figure 2.

and intermolecular H-bonds and short contacts. On the periphery of the cation, the $ampH^-$ molecules are H-bonded to the terminal EtOH molecules (O···O, ∼2.6 Å) and the NH_2 arm of another $ampH^-$ ligand bonded to the same Mn ion (N···O, ∼2.8 Å), while the nonbonded NH_2 arms of the centrally located amp^{2-} ions are H-bonded to the μ_3-bridging OH^- ions (O···O, ∼2.7 Å) and the I^- counterions (O···I, ∼3.5−3.8 Å). The latter interaction is propagated in all three directions in the crystal, directing the packing of the cations into sheets and chains (Figure 5). The closest intermolecular Mn···Mn distance in the same sheet is ∼7.2 Å, and the distance between adjacent sheets is ∼9.6 Å. $[Mn_{10}(OH)_6(aep)_4(aepH)_4I_4(EtOH)_4]I_4$ (**4**) has a structure analogous to that of **3** but crystallizes in the orthorhombic space group *Pbcn*. There are numerous intra- and intermolecular H-bonds and short contacts propagated in all three directions in the crystal, directing the packing of the cations (Figure 5). When viewed down the *c* axis, the molecules, each perpendicular to its nearest neighbor, form cross- or X-shaped columns. The closest intermolecular Mn···.Mn distance within the same sheet is ∼10.3 Å, and the distance between adjacent sheets is ∼10.3 Å.

$[Mn_{14}(OH)_2(Hpeol)_4(H_2peol)_6I_4(EtOH)_6]I_4$ (**5**) crystallizes in the monoclinic space group *P*21/*n* (Figure 6; selected bond lengths and angles are given in Table 2). The Mn−O core describes a planar "rectangular" disc of 14 Mn ions linked together by a combination of hydroxide and alkoxide ions to form a metallic skeleton of 14 edge-sharing triangles. The two central OH^- ions each bridge in a μ_3-fashion, while the tripodal ligands adopt three distinct coordination modes. Four are triply deprotonated ($Hpeol^{3-}$) and sit above and below the $[Mn_{14}]$ plane, bridging in an $\eta^3{:}\eta^3{:}\eta^3{:}\mu_6$-fashion. Six are doubly deprotonated (H_2peol^{2-}) and can be divided into two categories: four bridge across the long edges of the rectangle in an $\eta^2{:}\eta^2{:}\eta^1{:}\mu_3$-fashion, and two bridge across the short edges of the rectangle in an $\eta^2{:}\eta^2{:}\eta^1{:}\eta^1{:}\mu_3$-fashion. This is the first time the latter coordination mode has been seen. The central metal−oxygen core is thus $[Mn^{III}_6Mn^{II}_8(OH)_2(OR)_{24}]^{8+}$. The Mn ions are six-coordinate and in distorted octahedral geometries, with the Mn^{3+} ions displaying the usual Jahn−Teller elongations, each of which lies "parallel" to the short edges of the rectangle. Four terminally bound I^- ions and six EtOH molecules fill the vacant coordination sites on the Mn^{2+} ions. There are a significant number of intra- and intermolecular H-bonds: the terminal I^- ions are H-bonded to the terminally bonded O arms of H_2peol^{2-} ligands (I···O, ∼3.4 Å); the unbonded arms of the same ligands and the $Hpeol^{3-}$ ligands are H-bonded to the I^- counterions (O···I, ∼3.3 Å); and the O−H arms of H_2peol^{2-} ligands and terminal EtOH molecules are H-bonded to those on neighboring molecules (O···O, ∼2.6−2.8 Å). The result is an extensive,

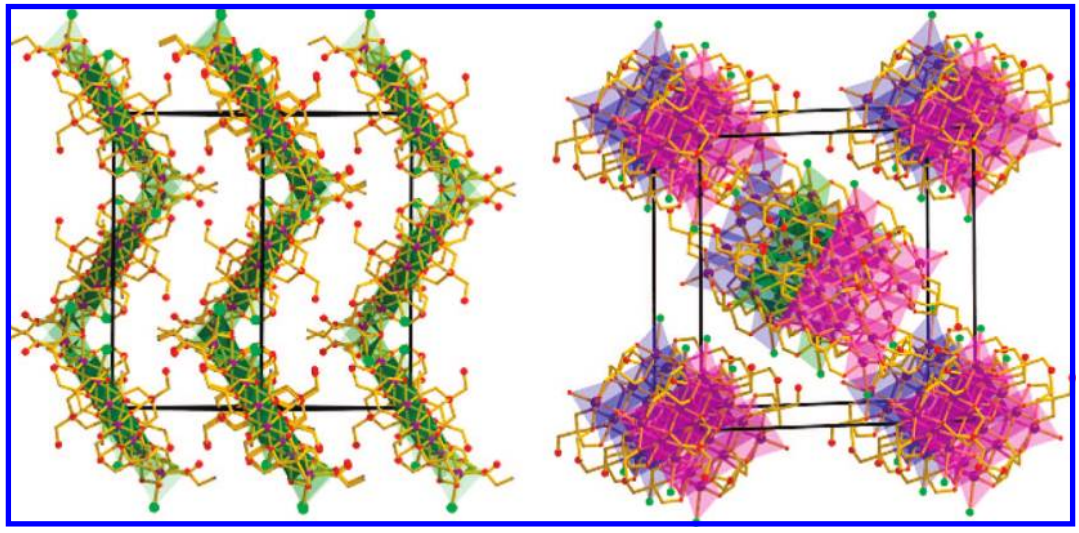

Figure 7. Packing of **5** in the crystal, viewed down the *b* axis (left) and the *a* axis (right).

Table 3. Bond Valence Sum Calculations for **1**−**5**

atom	$Mn^{(II)}$	$Mn^{(III)}$	$Mn^{(IV)}$	assignment	atom	$Mn^{(II)}$	$Mn^{(III)}$	$Mn^{(IV)}$	assignment
Complex **1**									
Mn1	1.88	1.75	1.71	(II)	Mn3	3.09	2.85	2.80	(III)
Mn2	2.02	1.88	1.84	(II)	Mn4	3.14	2.90	2.84	(III)
Complex **2**									
Mn1	2.05	1.91	1.87	(II)	Mn3	2.00	1.86	1.83	(II)
Mn2	3.09	2.85	2.80	(III)	Mn4	2.98	2.75	2.70	(III)
Complex **3**									
Mn1	3.46	3.19	3.13	(III)	Mn6	1.76	1.62	1.59	(II)
Mn2	1.78	1.64	1.61	(II)	Mn7	3.46	3.20	3.14	(III)
Mn3	3.45	3.19	3.13	(III)	Mn8	1.80	1.66	1.62	(II)
Mn4	1.79	1.65	1.62	(II)	Mn9	3.33	3.07	3.01	(III)
Mn5	3.45	3.18	3.12	(III)	Mn10	3.33	3.07	3.01	(III)
Complex **4**									
Mn1	3.41	3.16	3.10	(III)	Mn4	3.49	3.22	3.16	(III)
Mn2	1.81	1.67	1.63	(II)	Mn5	1.77	1.63	1.60	(II)
Mn3	3.38	3.12	3.06	(III)					
Complex **5**									
Mn1	1.72	1.58	1.55	(II)	Mn5	3.41	3.15	3.09	(III)
Mn2	2.14	1.97	1.94	(II)	Mn6	2.18	2.02	1.98	(II)
Mn3	3.48	3.20	3.14	(III)	Mn7	1.71	1.58	1.55	(II)
Mn4	3.34	3.08	3.02	(III)					

complicated H-bonded network of $[Mn_{14}]^{4+}$ cations throughout the crystal. The molecules of **5** pack in the commonly observed brick-wall pattern (Figure 7). In all cases, the oxidation states of the metal ions (and oxides/hydroxides) were assigned using a combination of charge balance, bond length considerations, and bond valence sum calculations (Table 3).[14]

Magnetic Studies. Magnetic susceptibility studies were carried out on powdered microcrystalline samples of **1**−**5** in the 300−0.3 K temperature range and for several applied fields. The field dependencies of **1** and **3** are essentially identical to those of **2** and **4**, respectively. Here we show the data for **1** and **3** only, in addition to **5** (Figure 9). For **1**, the room-temperature $\chi_M T$ value of approximately 48 cm^3 K mol^{-1} increases upon cooling to a maximum value of ∼224 cm^3 K mol^{-1} at 10 K before dropping to approximately 160 cm^3 K mol^{-1} at 1.8 K. The $\chi_M T$ value expected for an uncoupled $[Mn^{III}_6Mn^{II}_4]$ unit (g = 2.00) is approximately 36 cm^3 K mol^{-1}, less than the measured value at 300 K. For **3**, the room-temperature $\chi_M T$ value of ∼37 cm^3 K mol^{-1} gradually increases with decreasing temperature, reaching a maximum value of ∼79 cm^3 K mol^{-1} at ∼14 K, before falling rapidly to a value of ∼40 cm^3 K mol^{-1} at 2.0 K (Figure 9). For both complexes, the behavior is suggestive of dominant ferromagnetic exchange between the metal centers, resulting in a spin ground state S = 22 for both **1** and **3** (and similarly for **2** and **4**). The dramatic difference in the low-temperature maxima is assigned to a combination of intermolecular interactions and the weaker intramolecular exchange in the latter (vide infra). Ferromagnetic mixed-valent Mn clusters with nuclearity greater than four are exceptionally rare.[10n] For **5**, the room-temperature $\chi_M T$ value of ∼55.6 cm^3 K mol^{-1} collected for H = 1 kG is nearly constant down to ∼150 K, below which it starts falling, reaching a value of ∼24.3 cm^3 K mol^{-1} at 2.0 K (Figure 9). The expected (spin-only) value at 300 K is ∼53 cm^3 K mol^{-1}. The linear extrapolation of the ac susceptibility collected for 2 K < T < 20 K down to zero-temperature yields $S \simeq 7 \pm 1$.

In order to ascertain the spin ground states, magnetization data (M) were collected in the ranges 0−70 kG and 0.3−20 K;

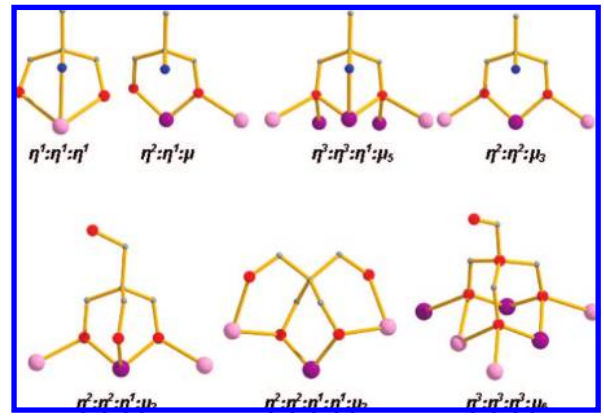

Figure 8. Coordination modes of $ampH_n^{(2-n)-}$ and $aepH_n^{(2-n)-}$ (top) and $H_npeol^{(4-n)-}$ (bottom) in **1**−**5**.

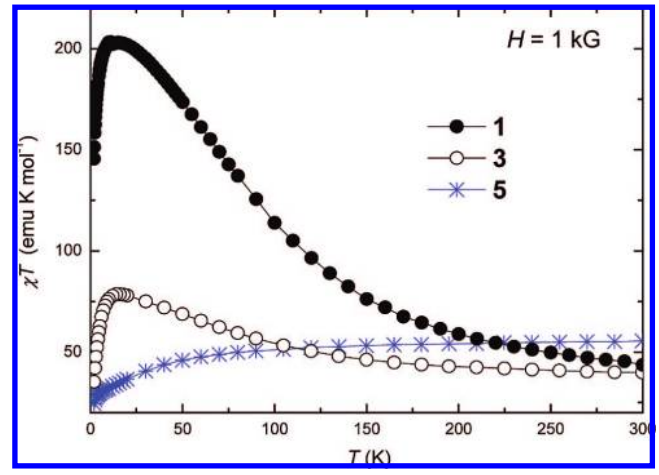

Figure 9. Plot of the $\chi_M T$ product vs temperature (T) for **1**, **3**, and **5** in the 300−1.8 K temperature range in an applied magnetic field of 1 kG. Solid lines are guides to the eyes.

the results are plotted in Figure 10. For **1**−**4**, the tendency toward parallel alignment of the Mn spins is corroborated by the large magnetization, exceeding 40 μ_B/f.u. at 70 kG and below ∼2 K. In particular for **1** and **2**, the fit of M by a matrix-diagonalization method affords the parameters S = 22, g = 2.0,

(14) (a) Brown, I. D.; Altermatt, D. *Acta Crystallogr. B* **1985**, *41*, 244–247. (b) Zhang, X. Y.; O'Connor, C. J.; Jameson, G. B.; Pope, M. T. *Inorg. Chem.* **1996**, *35*, 30–34. (c) Thorp, H. H. *Inorg. Chem.* **1992**, *31*, 1585–1588.

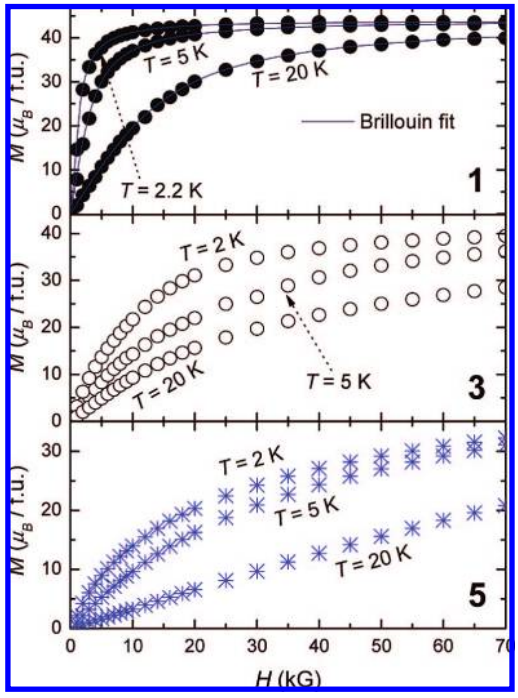

Figure 10. Magnetization (M) vs field (H) for **1**, **3**, and **5** in the indicated temperature and field ranges. For **1**, solid lines are the Brillouin fits.

and $D = 0$ cm^{-1}. Given the molecular symmetry (approximately T_d) of the complex, a value for the zero-field splitting of, or close to, zero is expected. Thus, despite the large S value, complex **1** (and **2**) does not behave as a single-molecule magnet, as confirmed by the lack of an out-of-phase (χ''_M) signal in ac susceptibility studies. The low-temperature in-phase $\chi'_M T$ vs T data are superimposable on the dc data. The negligible anisotropy suggests that the decrease in $\chi_M T$ below 10 K (Figure 9) is likely assigned to weak intermolecular antiferromagnetic interactions, consistent with the "dimeric" $[Mn_{10}]_2$ structure in the crystal. For **3** and **4**, the magnetization measurements cannot be described solely by Brillouin curves corrected for finite magnetic anisotropies (Figure 10). The same holds for **5**, whose magnetization achieves saturation values (i.e., 32 μ_B/f.u. for 2 K and 70 kG) consistent with large field-stabilized spin states (Figure 10). As we shall infer below from the specific heat experiments, the field dependencies of **3**−**5** are complicated by the influence of (many) low-lying excited S states, whose occupancy strongly depends on the applied magnetic field.

Experiments at temperatures below 2 K reveal different behaviors for the investigated complexes. The specific heat C of **1** shows a broad anomaly that shifts toward higher temperatures on increasing applied field (Figure 11). At much higher temperatures, the lattice contribution dominates over the magnetic one, and the experimental specific heat increases constantly with temperature. The magnetic contribution to $C(T,H)$ for $H \geq 10$ kG is due to Schottky-type Zeeman splitting of the otherwise degenerate ($D = 0$ cm^{-1}) energy spin states. The fit (solid lines in Figure 11) of the experimental data to the calculated Schottky curves is excellent and provides $S = 22$, $g = 2$, and $D = 0$ cm^{-1}, in agreement with the $M(H)$ data. Given that $[Mn_{10}]_2$ dimers are formed, one would expect that the appearance of an exchange field acting on each molecule that, similar to the external applied field, causes a Zeeman splitting of the molecular spin ground state. This shows up in the experimental C collected at zero applied field that follows the

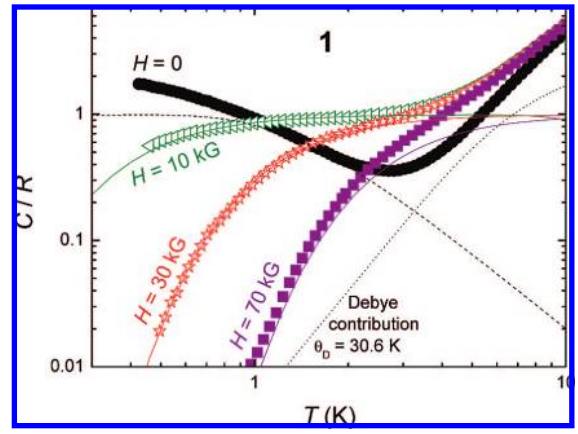

Figure 11. Specific heat (C) normalized to the gas constant (R) vs temperature (T) for **1** at several applied fields. The solid and dashed lines are the fits to the Schottky contributions (see text); the dashed line is the Debye fit of the lattice contribution.

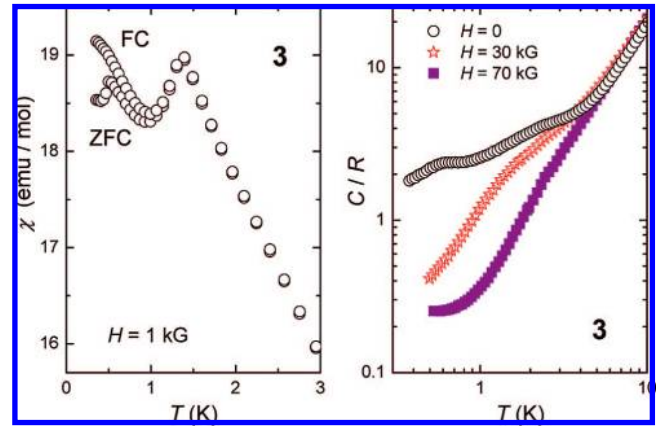

Figure 12. (Left) Dc susceptibility vs T for **3** collected for $H = 1$ kG in the zero-field-cooled (ZFC) and field-cooled (FC) regimes. (Right) Specific heat normalized to the gas constant vs T for **3** collected for $H = 0$, 30, and 70 kG, as labeled.

Schottky behavior (dashed line, Figure 11) calculated for $S = 22$, $g = 2$, and $D = 0$ cm^{-1}, and an exchange field $H_{ex} = 820$ G down to 1 K. For decreasing temperatures below 1 K, the intermolecular correlations become dominant, overwhelming the single-molecule behavior, and the experimental C keeps increasing down to the minimum temperature accessible by our instrument. From the estimate of H_{ex}, and given that $g\mu_B H_{ex} S = nJS^2$, we obtain the absolute value of $nJ \approx 5$ mK for the intermolecular exchange coupling.

For **3**, zero-field-cooled (ZFC) and field-cooled (FC) magnetic susceptibility measurements for $H = 1$ kG reveal a sharp feature at about 1.4 K as well as an additional peak at the much lower temperature of ~0.5 K, accompanied by magnetic irreversibility (Figure 12). A peak in the susceptibility can be accounted for by (i) a magnetic phase transition or (ii) superparamagnetic blocking of the molecular spins. For a phase transition to occur, however, one would expect the specific heat to detect a *sharp* anomaly at the ordering temperature.[2] No such critical feature is experimentally seen; rather, *smooth* and *broad* anomalies are seen at the corresponding temperatures in the specific heat (Figure 12). Their presence is likely associated with different crystallographic forms of **3**. Four of the six Mn^{III} ions within the cluster core experience a Jahn−Teller (JT) elongation, and two experience a JT compression.[10op] However, only Mn9 and

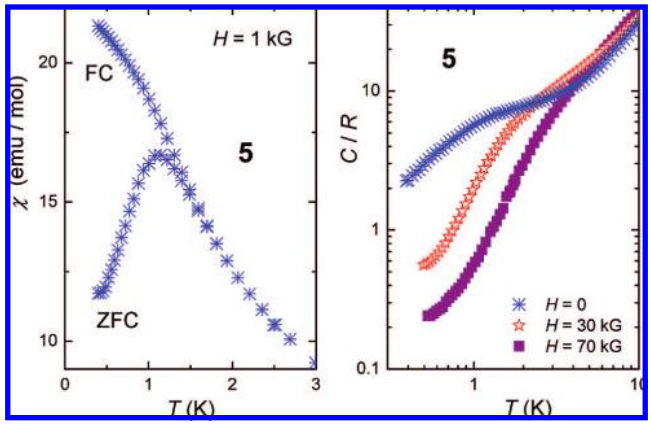

Figure 13. (Left) Dc susceptibility vs T for **5** collected for $H = 1$ kG in the zero-field-cooled (ZFC) and field-cooled (FC) regimes. (Right) Specific heat normalized to the gas constant vs T for **5** collected for $H = 0$, 30, and 70 kG.

Mn10 reside "within" the core (Figure 4), the others surrounding the periphery of the molecule, and their JT elongations/compressions are likely sensitive to change/disorder. For **3**, this results in JT isomerism,[15] i.e., two or more molecules differing in the relative orientation of one or more JT axes. Therefore, not all molecules are magnetically equivalent because of different spin states and/or anisotropies, yielding multiple superparamagnetic relaxation processes, thence multiple peaks in the susceptibility.[16]

We performed similar FC and ZFC measurements at 1 kG for **5**, finding that magnetic irreversibility develops below ~1 K (Figure 13). As for **3**, the specific heat rules out a phase transition as the possible reason for the susceptibility peak. Indeed, a broad bump is reported in the specific heat (Figure 13), which is the Schottky-like anomaly normally encountered in superparamagnets. This shows up at zero applied field because the crystal field splits the electronic levels, which are then further split by the applied field, causing the bump to move toward higher T for increasing field. We conclude that **5** behaves as a superparamagnet, and given that the blocking temperature T_B is typically 1/18 of the effective anisotropy barrier U,[17] we finally obtain an estimate of $U'' = 18$ K for **5**. We refrain from estimating the molecular anisotropy because (anticipating the discussion below) the magnetic relaxation likely proceeds via excited spin states.

Contrary to the results for **1**, we note that for **3** and **5** (and hence **2** and **4**) no simple model of the magnetic contribution to the specific heat can be employed. It is straightforward to realize that the zero-field C of **3** and **5** is excessively large for temperatures below ~2 K, i.e., a temperature range in which the lattice contribution is negligible. Typical values should not exceed ~1−2) R, as in **1**, provided that intermolecular interactions are absent.[2] The excess of magnetic specific heat in **2**−**5** must therefore arise from the presence of low-lying spin states other than the ground state. As we shall see in what follows,

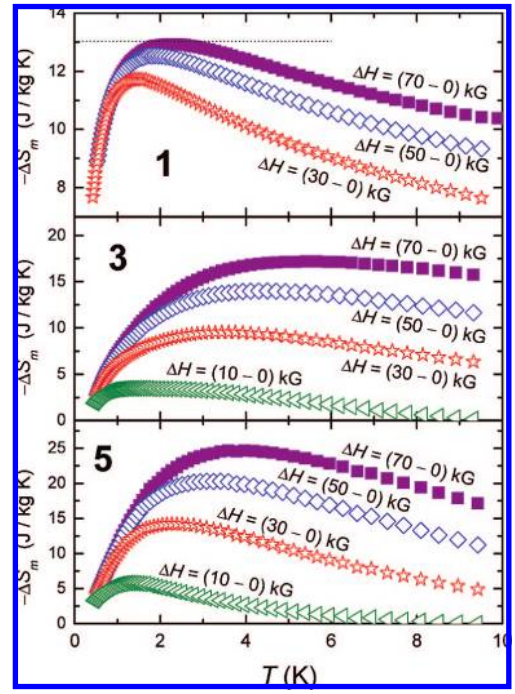

Figure 14. Magnetic entropy changes ($-\Delta S_m$) vs T as obtained from the measurements of C in the indicated applied field changes (ΔH) for **1**, **3**, and **5**. Dotted line in the top panel is the limiting value of $R \ln(2S + 1)$ for $S = 22$ (see text).

these accessible excited spin states have an *enormous* implication for the enhancement of the magnetocaloric effect (MCE).

The entropy of magnetic materials is intimately related with their capability of magnetic cooling through the MCE,[3] i.e., the change of the magnetic entropy ΔS_m upon a change in the applied magnetic field ΔH. The larger ΔS_m for a given ΔH, the better performance the investigated complex has in as a refrigerant material. From the experimental specific heat C data of the investigated complexes (Figures 1113), we calculate $\Delta S_m(T,H) = \int[C(T,H_f) - C(T,H_i)]/T \, dT$ for selected field changes $\Delta H = H_f - H_i$. Note that the estimation of the lattice contribution to the specific heat is irrelevant for our calculations, since we deal with differences between total entropies at different H. The so-obtained temperature dependencies of ΔS_m for **1**, **3**, and **5** are depicted in Figure 14 for several ΔH values. As for **1**, it can be seen that $-\Delta S_m$ reaches a maximum value of 13.0 J kg^{-1} K^{-1} (or equivalently 3.8R) at ~2.2 K for $\Delta H =$ 70−0 kG. This value corresponds to the full change of the total magnetic entropy $R \ln(2S + 1)$ for a spin $S = 22$ (dotted line in the top panel of Figure 14) and is one among the highest values ever reported for this temperature range.[2] Complexes **2**−**5** possess large field-stabilized spin states, as well as the presence of several excited spin states that are thermally accessible even at very low temperatures. This leads to an excess of magnetic entropy. Adding this extra contribution to the magnetic entropy effectively results in a MCE enhancement. For the maximum investigated $\Delta H = 70-0$ kG, we observe that $-\Delta S_m$ reaches the maximum value of 17.0 J kg^{-1} K^{-1} (equivalent to 5.4R) at ~5.2 K for **3**, whereas **5** is even more impressive, achieving a remarkable value of 25 J kg^{-1} K^{-1} (equivalent to 10.2R) at ~3.8 K. Both of these values notably exceed the respective ones expected if ΔS_m were determined *just* by the spin ground state, as in **1**. Let us assume, for instance, that **3** has a spin ground state $S = 22$. Without the degrees of freedom added from the other spin states, $-\Delta S_m$ cannot theoretically amount to more

(15) Sun, S; Ruiz, D.; Dilley, N. R.; Soler, M.; Ribas, J.; Guzei, I. A.; Rheingold, A. L.; Folting, K.; Maple, M. B.; Christou, G.; Hendrickson, D. N. *Chem. Commun.* **1999**, 1973–1974.
(16) Aubin, S. M. J.; Sun, Z.; Eppley, H.; Rumberger, E. M.; Guzei, I. A.; Folting, K.; Gantzel, P. K.; Rheingold, A. L.; Christou, G.; Hendrickson, D. N. *Inorg. Chem.* **2001**, *40*, 2127–2146.
(17) Evangelisti, M.; Candini, A.; Ghirri, A.; Affronte, M.; Powell, G. W.; Gass, I. A.; Wood, P. A.; Parsons, S.; Brechin, E. K.; Collison, D.; Heath, S. L. *Phys. Rev. Lett.* **2006**, *97*, 167202.

than $R \ln(2S + 1) = 13.0$ J kg^{-1} K^{-1} for this spin value—notably smaller than what is experimentally observed. We stress that the values reported in Figure 14 are exceptionally impressive: to our knowledge, no other refrigerant material shows values as large as $-\Delta S_m = 25$ J kg^{-1} K^{-1} for $\Delta H = 70-0$ kG in the liquid helium T range.[2–5]

Conclusions

In conclusion, our intial investigations into the coordination chemistry of ampH$_2$ and the closely related aepH$_2$ and H$_4$peol ligands have afforded beautiful and unusual mixed-valent decametallic Mn supertetrahedra and discs and a tetradecametallic disc. Complexes **1**−**3** are the first characterized Mn clusters containing the amp^{2-} ligand. Magnetic studies reveal complexes **1**−**4** to possess extremely large spin grounds state of $S = 22$ as a result of the dominant ferromagnetic exchange interactions between the metal centers, thus making them part of a select and illustrious band of molecules displaying this unusual combination. All five complexes show enormous magnetocaloric effect: **1** and **2** as a result of negligible zero-field splitting of the maximum possible ground state, and **3**−**5** as a result of possessing a high spin degeneracy at finite low temperatures. The investigation of novel molecular clusters with a high spin degeneracy at finite low temperatures opens the way to important improvements in the MCE of molecular complexes, and this ultimately facilitates their use in magnetic cooling applications. To this end, the complexes described above are the very best cooling refrigerants for low-temperature applications. Furthermore, they suggest a new synthetic strategy for obtaining novel molecules with even larger MCE: the introduction of ions (and ligands) that will promote weak ferro- or ferrimagnetic interactions, leading to high spin ground states and easily accessible (low-lying), degenerate, excited states with large S values.

Acknowledgment. The authors acknowledge the EPSRC and Leverhulme Trust (UK) and MAGMANet (NMP3-CT-2005-515767).

Supporting Information Available: Crystallographic details in CIF format. This material is available free of charge via the Internet at http://pubs.acs.org.

JA802829D